RESEARCH ARTICLE

ADVANCED
INTELLIGENT
SYSTEMS
Open Access

www.advintellsyst.com

Dynamic Tuning of Plasmonic Hot-Spot Generation through Cilia-Inspired Magnetic Actuators

Gorkem Liman, Emre Ergene, Emrecan Yildiz, Kubra Ozkan Hukum, Pinar Yilgor Huri, Arif E. Cetin,* Hakan Usta,* and Gokhan Demirel*

Soft actuators that draw inspiration from nature are powerful and versatile tools for both technological applications and fundamental research, yet their use in hot-spot engineering is very limited. Conventional hot-spot engineering methods still suffer from complexity, high process cost, and static generation of hot-spots, thus, underperforming particularly in the application side. Herein, we demonstrate a strategy based on plasmonic nanoparticles decorated cilia-inspired magnetic actuators that enable highly accessible millimeter-sized hot-spot generation via bending motion under a magnetic field. The hot-spot formation is shown to be reversible and tunable, and leads to excellent Raman signal enhancements of up to ≈120 folds compared to the unactuated platforms. Accessible electromagnetic field magnification in the platforms can be manipulated by controlling magnetic field strength, which is further supported by finite difference time domain (FDTD) simulations. As a proof-of-concept demonstration, a centipede-inspired robot is fabricated and used for sample collection/analysis in a target environment. Our results demonstrate an effective strategy in soft actuator platforms for reversible and tunable large-area hot-spot formation, which provides a promising guidance toward studying the fundamentals of hot-spot generation and advancing real-life plasmonic applications.

1. Introduction

The nondestructive identification and analysis of molecular species with high selectivity and sensitivity are of great research interest for use in various applications ranging from medical diagnostics[1,2] to environmental sampling[3,4] and anticounterfeiting.[5,6] Raman spectroscopy stands out as an important technique for this purpose, which is based on inelastic scattering of photons from molecules of interest and carries unique, fingerprint-like structural information.[7–9] Especially, sample preparation is straightforward, and specific electronic excitation is not required in Raman analyses, which makes this spectroscopic technique a highly versatile tool for almost any chemical structure. However, conventional Raman spectroscopy has an inherent limitation arising from extremely low cross-sections (typically 10^{-29}–10^{-30} cm^2) for the desired inelastic scattering.[9–12] To this end, the discovery of surface-enhanced Raman spectroscopy (SERS) in the 1970s and the advent of nanotechnology in the past few decades have led to the development of unprecedented plasmonic substrates with highly sensitive molecular detection properties. Today, electromagnetic enhancement (EM) mechanism is considered to be the most important effect for Raman signal enhancement in plasmonic SERS substrates, which relies on excitation of localized surface plasmon resonances (LSPRs) leading to the localization and magnification of the incident electromagnetic field in regions called hot-spots.[13–15] Especially, sensing ultralow concentrations and reaching a single molecule detection level on a SERS substrate require rationally engineered hot-spots with small interparticle distances (<10 nm). In the last two decades, although some bottom-up/top-down nanofabrication techniques (e.g., e-beam lithography, focus ion beam lithography, and DNA origami) have been employed to control and tune hot-spot generations,[16–19] these techniques require high-cost/complex instrumentation and fabrication steps, and the

G. Liman, E. Ergene, E. Yildiz, K. O. Hukum, G. Demirel
Bio-inspired Materials Research Laboratory (BIMREL)
Department of Chemistry
Gazi University
06500 Ankara, Turkey
E-mail: gdemirel@gazi.edu.tr

The ORCID identification number(s) for the author(s) of this article can be found under https://doi.org/10.1002/aisy.202200420.

E. Ergene, P. Yilgor Huri
Department of Biomedical Engineering
Faculty of Engineering
Ankara University
06135 Ankara, Turkey

A. E. Cetin
Izmir Biomedicine and Genome Center
35340 Izmir, Turkey
E-mail: arifengin.cetin@ibg.edu.tr

H. Usta
Department of Nanotechnology Engineering
Abdullah Gül University
38080 Kayseri, Turkey
E-mail: hakan.usta@agu.edu.tr

**ADVANCED
SCIENCE NEWS**
www.advancedsciencenews.com

**ADVANCED
INTELLIGENT
SYSTEMS**
Open Access
www.advintellsyst.com

hot-spots generated are typically submicron to micron-sized. Today, the design and fabrication of rationally positioned/spaced millimeter-sized hot-spots on a large-area SERS platform with high uniformity and reproducibility still remain a major challenge.[20–22] Especially, using facile fabrication methods (e.g., polymer casting into a 3D printed mold) and dynamic control of the hot-spot generation with good resolution by using a localized external stimulus (e.g., magnetic field) could be very advantageous for real-life applications. Exploring novel approaches to control and manipulate hot-spot generations over sizeable areas is important not only to widen the scope of SERS platforms in molecular sensing applications but also to reveal hot-spot-based Raman enhancement mechanisms.

Soft materials and actuators offer a great potential for broader hot-spot engineering applications that are not possible using conventional rigid materials and systems. Inspired by natural creatures with functional soft bodies, numerous soft actuators have been fabricated and employed for a diverse range of applications including medical devices,[23,24] soft grippers,[25,26] sensors,[27–29] wearables,[30,31] and artificial muscles.[32,33] Among various methods, applying an external magnetic field to create a torque or force on the soft actuator is one of the simplest yet effective actuation approaches.[34–44] More importantly, this actuation method is transparent and noninvasive, and high temporal resolution is possible by controlling the amplitude, gradient, and direction of the magnetic field. Although some interesting studies on sample capturing and trapping have been reported using soft actuator platforms,[45–47] their use in hot-spot engineering is still very limited. Considering the great potential and advantages of soft actuators, we recently demonstrated that the irreversible folding of a prestrained polystyrene (PS) sheet decorated with plasmonic structures enables hot-spot formation by controlling the temperature distribution on the material.[48] The fabricated platforms were able to demonstrate a Raman signal enhancement as large as ≈70-fold due to folding of their arms. However, irreversible folding behavior of PS sheet, possibility of thermal degradation of analyte molecules during folding process, and limited generation and distribution of hot-spots on platforms are the main drawbacks of this platform. In light of the aforementioned discussions and motivations on hot-spot engineering, we now envision that a magnetic actuation approach can be developed to engineer reversible large-area accessible hot-spot formations and to tune light-matter interactions via electromagnetic field enhancements for use in real-life plasmonic applications.

Here, we demonstrate a strategy to realize reversible and tunable plasmonic hot-spot formation in cilia-inspired magnetic actuators. The magnetic actuators are made up of Ecoflex and micron-sized magnetic Fe particles, and they were fabricated using 3D-printed molds to give two closely positioned millimeter-long cylindrical or truncated conical arms. The arms were decorated with plasmonic Au NPs (diameter ≈ 20 nm) to enable hot-spot formation upon bending under a permanent magnetic field. The hot-spot generation performances of the new actuator platforms were evaluated via SERS using varied reporter molecules and also by employing 2D and 3D confocal Raman mapping techniques. Experimental investigations and finite difference time domain (FDTD) simulations clearly demonstrate that the current cilia-inspired magnetic actuators enable highly accessible millimeter-sized hot-spot generation under a magnetic field and lead to excellent Raman signal enhancements up to ≈120-fold compared to the unactuated platforms. Accessible electromagnetic field magnification in these platforms was also shown to be tuned by the magnetic field strength. To show the potential of our proposed strategy, a centipede-inspired robotic platform was fabricated for analyte capturing and analysis in a target environment.

2. Results and Discussion

The initial version of the magnetic actuator platforms developed in our study is designed having two closely positioned cylinders with a micron-sized diameter (400 μm) (**Figure 1**). The lengths of the cylinders are either 4.0 or 5.0 mm, and the distance between them is varied as 1.6, 2.0, and 2.4 mm to manipulate the area at joint points for detailed investigations. In the fabrication of these platforms, the molds were first designed using the 3D Builder software and then prepared with a 3D printer using PLA filaments (step 1 in Figure 1a). After printing, all supporting materials were removed from the mold, and a thin layer of lubricant was applied (step 2 in Figure 1a). In the next step, a mixture (1:0.3 weight ratio) of Ecoflex (00–30) and magnetic Fe particles (≈5.0 μm in diameter) was filled into the mold and cured in an oven ($T = 70\,°C$) (step 3 in Figure 1a). Finally, the magnetic actuator platforms were peeled off the molds showing no observable damage with respect to the original design.

To evaluate the actuating performance of our platforms, we used a permanent magnet (NdFeB) with a magnetic field strength of 0.12 T that approached the platform from underneath the support surface between the cylinders in a direction parallel to the cylinder long axis (step 5 in Figure 1a). In the presence of a permanent magnetic field, all fabricated platforms, as expected, exhibit reciprocal motion to form bent states making a physical contact with each other as shown in Figure 1b (for 5 mm-long cylinders) and c (for 4 mm-long cylinders) (Movie S1, Supporting Information). When the magnetic field is removed, the cylinders go back to their initial states. The durability of the platforms (for 5 mm-long cylinders) was evaluated under a magnetic field strength of 0.12 T [a periodic magnetic field on (5 s)/off (5 s) cycles]. It is observed that, even after 1000 cycles, the platforms still maintained the original movement without any important distortion, indicating excellent durability (Figure S1, Supporting Information). For similar magnetic platforms, dynamic motion of the cylinders has also been reported by using Cosserat rod model.[36,49] For both platforms, different joint angles (α) between the cylinders were observed depending on the distance between the cylinders. For 4 mm-long cylinders, the joint angle was measured as $32 \pm 3.4°$ when the distance was 1.6 mm, which gradually increased to $44 \pm 4.7°$ and $52 \pm 5.6°$ when the distance was increased to 2.0 and 2.4 mm, respectively (Figure 1d). For the platform with 5 mm-long cylinders, the joint angles were found to be 10–20% smaller as $26 \pm 2.8°$ for 1.6 mm distance, $38 \pm 3.3°$ for 2.0 mm distance, and $46 \pm 4.2°$ for 2.4 mm distance (Figure 1d). The lowest joint angle obtained for 5 mm-long cylinders with 1.6 mm distance yields the formation of the highest contact surface between the cylinders, which is expected to maximize the area and
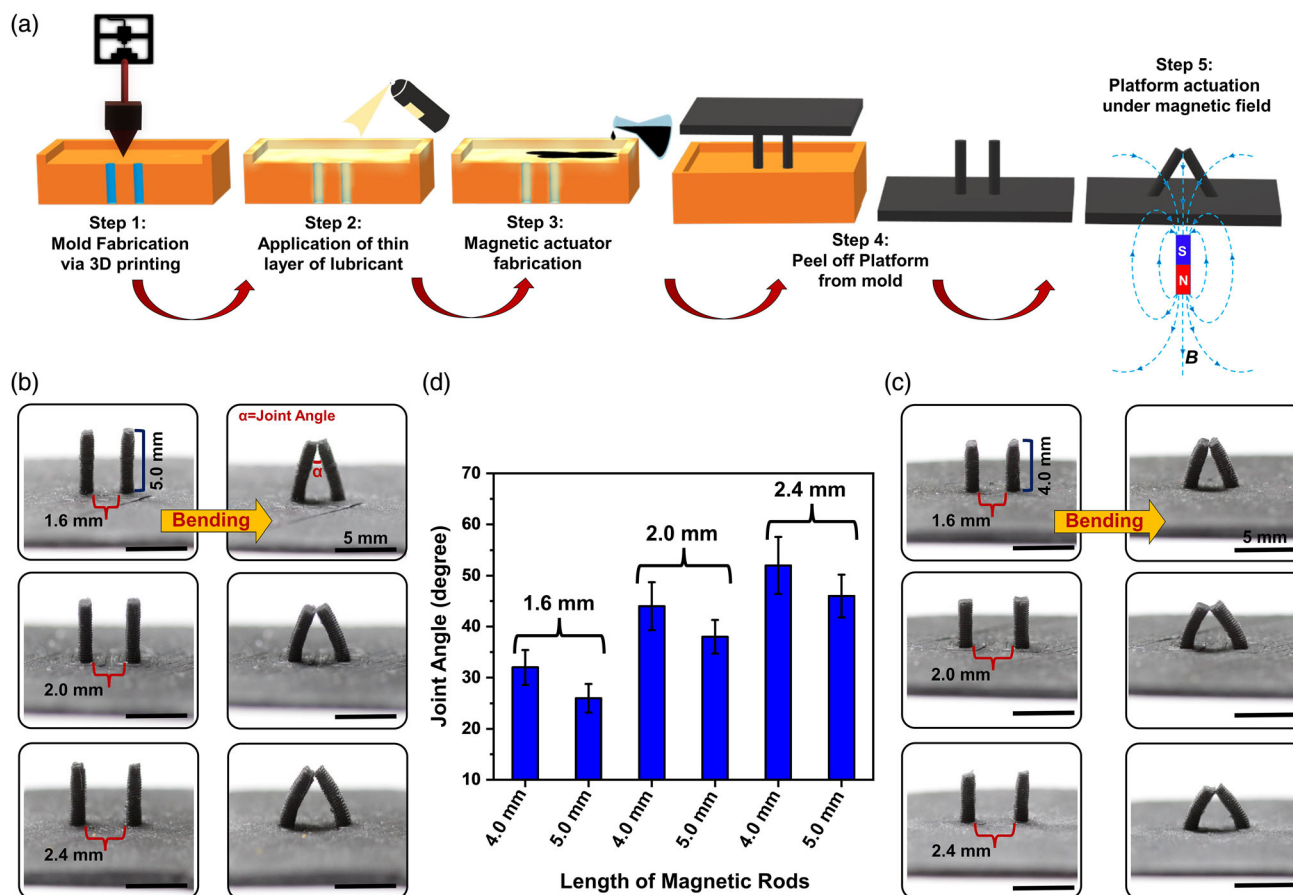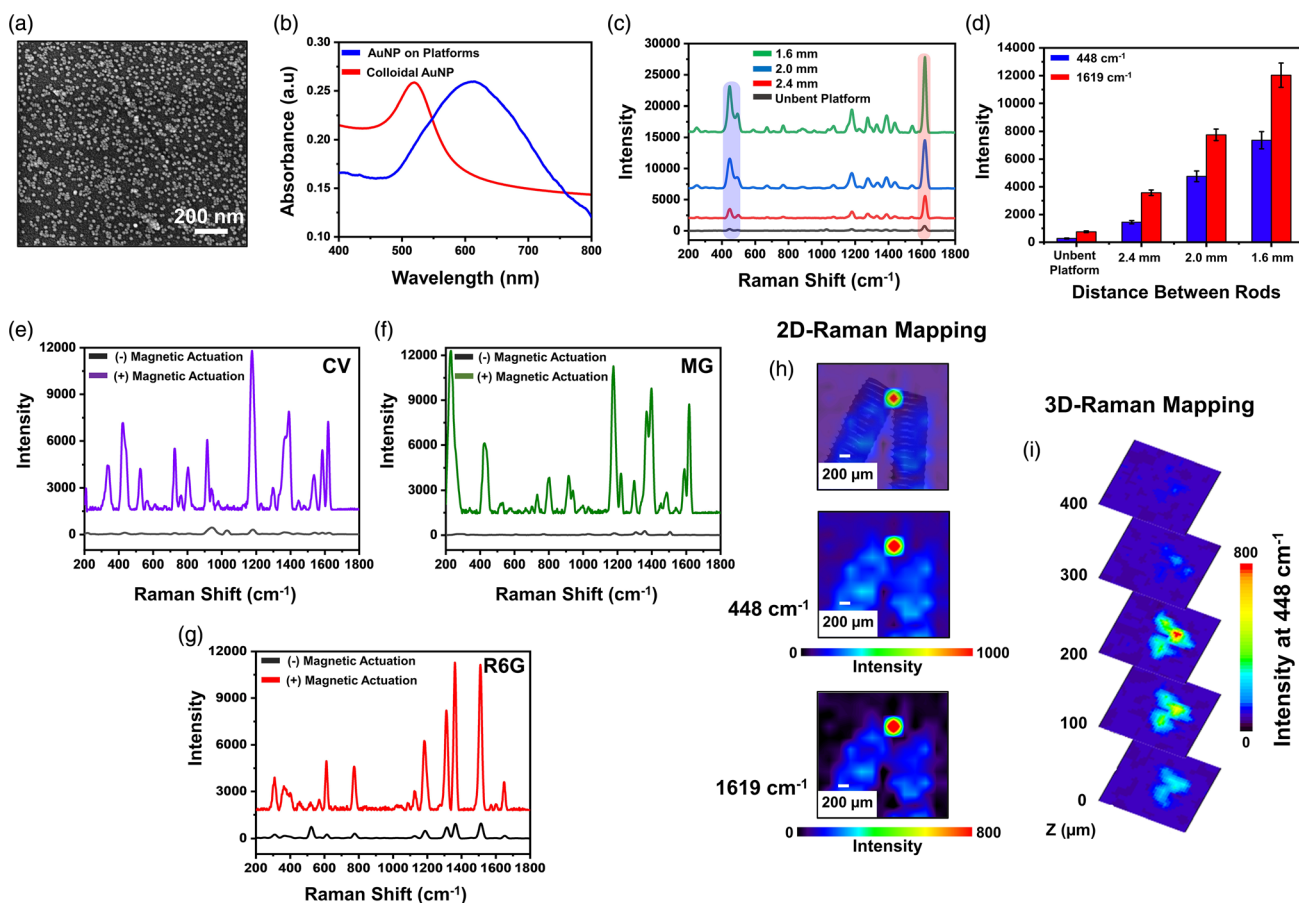
Figure 1. Fabrication and bending performance of cylindrical magnetic actuator platforms. a) Schematic illustration for the fabrication steps of cylindrical magnetic actuator platforms (steps 1–4) and the magnetic actuation process under magnetic field (step 5). b,c) Snapshots of the bending performance of cylindrical magnetic actuator platforms with different lengths and distances under 0.12 T magnetic field. Scale bar: 5 mm. d) Variation of the joint angles for cylindrical magnetic actuator platforms as a function of cylinder length and distance.

strength of available hot-spots in these platforms. Therefore, further decoration with plasmonic nanoparticles and molecular sensing experiments in this study were performed with this particular actuator platform.

The magnetic actuator platforms were decorated with plasmonic gold nanoparticles (AuNPs) with a diameter of ≈ 20 nm to evaluate their hot-spot formation performances under a magnetic field. The spherical AuNPs were first prepared by well-established Turkevich method.[50] To have a homogenous and robust AuNP layer, a thin layer (≈ 10 nm) of polydopamine (PDOP) was first applied on the cylindrical platforms.[51,52] Also, on the basis of our previous experiments, 24 h immersion time into an aqueous AuNPs solution was employed.[48] **Figure 2**a shows the SEM image of a AuNP decorated cylinder. The AuNP density on the cylinder surface was calculated to be 4.48×10^{10} nanoparticle cm^{-2}, which indicates a highly favorable morphology for hot-spot formation during physical contact. The optical characterization of AuNP decorated platforms was also performed by UV–vis absorption spectroscopy. As shown in Figure 2b, the LSPR absorption maximum for the new platform was observed at 611 nm, which is significantly red-shifted with respect to that of as-synthesized AuNPs in solution

($\lambda_{\max} = 519$ nm), most likely a result of dense AuNP film formation on the platforms.

The hot-spot formation properties of the new platforms were investigated using SERS analyses. In these experiments, four different Raman reporter molecules [i.e., methylene blue (MB), rhodamine 6G (R6G), crystal violet (CV), and malachite green (MG)] were used, and their aqueous solutions (1×10^{-3} M) were drop-casted onto one side of the AuNP decorated cylinders to eliminate any potential concentration effect upon platform bending. All SERS analyses were performed using a Raman laser excitation wavelength of 785 nm (1.58 eV) at which the Raman reporters or the polymeric substrate exhibits no electronic transitions.[53–55] Therefore, chemical contributions to Raman signal enhancement originating from pure analyte or substrate–analyte electronic excitations could be eliminated in our evaluations. First, Raman spectrum of MB was collected from the platform before applying magnetic field (black spectrum in Figure 2c). The fingerprint Raman peaks were identified at 448 cm^{-1} for (C—N—C) skeletal deformation, 1181 cm^{-1} for (C—N) stretches, 1394 cm^{-1} for asymmetric/symmetric (C—H) ring stretches, and 1619 cm^{-1} for (C—C) ring stretches. It is noteworthy that the underlying polymeric platform has an intrinsic

ADVANCED
SCIENCE NEWS

www.advancedsciencenews.com

ADVANCED
INTELLIGENT
SYSTEMS

www.advintellsyst.com

Figure 2. Cylindrical magnetic actuator platforms and SERS performances. a) SEM image of an AuNP-decorated cylindrical magnetic actuator platform (Scale bar: 200 nm). b) UV–vis absorption spectra of as-synthesized AuNPs (shown in red) in solution and AuNP-decorated cylindrical magnetic actuator platforms (shown in blue). c) SERS spectra of MB (10^{-3} M) at the joint point of cylindrical magnetic actuators with different distances between the cylinders under 0.12 T magnetic field. d) Raman intensity histograms of the 448 and 1619 cm^{-1} peaks derived from the SERS spectra shown in (c). e–g) SERS spectra of CV, MG, and R6G analyte molecules on the cylindrical platforms (1.6 mm distance) in the presence and absence of magnetic field (0.12 T). For all experiments, analyte concentrations were 10^{-3} M. h) 2D SERS Raman mapping of the bent cylindrical platforms for the 1619 and 448 cm^{-1} peaks of MB (The first figure is the overlaying figure that was produced using real platform pictures obtaining from Raman microscope and 2D SERS Raman mapping of the collected analyte molecules on the platforms for the 448 cm^{-1}). i) 3D Raman spatial mapping of the bent cylindrical platform showing different focal planes along the z-axis.

Raman spectrum originating from PDOP coating and Ecoflex; however, due to high Raman cross-section of MB, these low-intensity Raman signals were mostly suppressed in the observed spectra (Figure S2 and S3, Supporting Information). In the presence of a permanent magnetic field, the cylindrical arms on the platform bent toward each other and demonstrated a remarkable hot-spot generation at the physical contact point (Figure 2h). As a result, a dramatic Raman signal enhancement for each characteristic Raman peak of MB was identified in the collected spectra. For the platform with 2.4 mm of distance between the cylinders, the peak intensities observed at 448 and 1619 cm^{-1} were increased by 5.4 and 4.8-fold as compared to the original unbent platform (Figure 2d). The same enhancements were increased to 17.7-fold (for 448 cm^{-1}) and 10.3-fold (for 1619 cm^{-1}) for the platform with 2.0 mm distance, and 26.6-fold (for 448 cm^{-1}) and 16.1-fold (for 1619 cm^{-1}) for the platform with 1.6 mm distance (Figure 2d). This is a direct result of the increased physical contact area between the cylindrical arms upon reducing the

distance, which allows for the deposition of larger number of probe molecules and better enhancement of the electromagnetic field in the hot-spot region. The hot-spot formation properties were further evaluated using the other Raman reporters CV, R6G, and MG. As shown in the corresponding Raman spectra of these molecules (Figure 2e–f), similar strong enhancements were observed with these reporter molecules as well when a magnetic field is applied. For CV and MG, (C—H) in-plane bending vibration peaks at 1175 cm^{-1} were enhanced about 25- and 84-fold, respectively, after magnetic actuation. Ring deformation peak at 1180 cm^{-1} for R6G was also increased by 12-fold in the presence of magnetic field. This indicates not only that the significant electromagnetic field enhancement observed in the hot-spots is effective for varied molecular structures but also that the enhancements have a potential to be further increased in different probe molecules. Strong light–matter interactions provide large local electromagnetic fields, which could be accessible by nearby analyte molecules to yield enhanced Raman

signals.[56,57] While in the absence of a magnetic field, these large nearfields are generated only in a small region between plasmonic nanoparticles, in the presence of magnetic field, hot-spot generation occurs at joint points and spreads over a much wider region. Here, we note that all Raman investigations were carried out under the same experimental conditions (i.e., illumination area and Raman configurations) for both bent and unbent platforms. In addition, LSPR wavelength shift after the bending process could only have a minor role in the enhancement mechanism, as we previously demonstrated.[48]

To gain insights into the hot-spot generations in these platforms, we investigated the platforms in the bent-state using a Confocal Raman Microscope with a mapping software (785 nm laser, 10× objective) (Figure 2h). In the mapping process, more than 1000 Raman spectra were collected starting from the outside and going toward the center of the joint. The 2D Raman mapping shows that the Raman signals of MB at 448 and 1619 cm^{-1} gradually increase going from outside to the center of the joint point, demonstrating an obvious hot-spot

generation at the physical contact point. For the bent platform, we also performed the Raman spatial mapping of the 448 cm^{-1} peak on different planes along the z-axis (Figure 2i), which again shows the largest enhancements at the joint point over a thickness of ≈100–200 μm along the z-axis.

To tune and optimize the joint point characteristics in the magnetic actuators, we designed and fabricated a modified version of our platform with two truncated conical arms (1.6 mm distance) having diameters of 0.4 mm and lengths of 4.0 mm. This design is envisioned to enhance the physical contact area in both lateral and vertical directions, which correspondingly could facilitate further enhancement of the electromagnetic field for very efficient hot-spot formation. **Figure 3**a shows the SEM image of the fabricated conical magnetic platform and snapshots of its bending performance under 0.12 T magnetic field. Although the conical platform exhibits a similar reciprocal motion to the cylindrical one, they form a higher contact area under magnetic field due to soft sharp tips (Movie S2, Supporting Information). This simple design difference provides
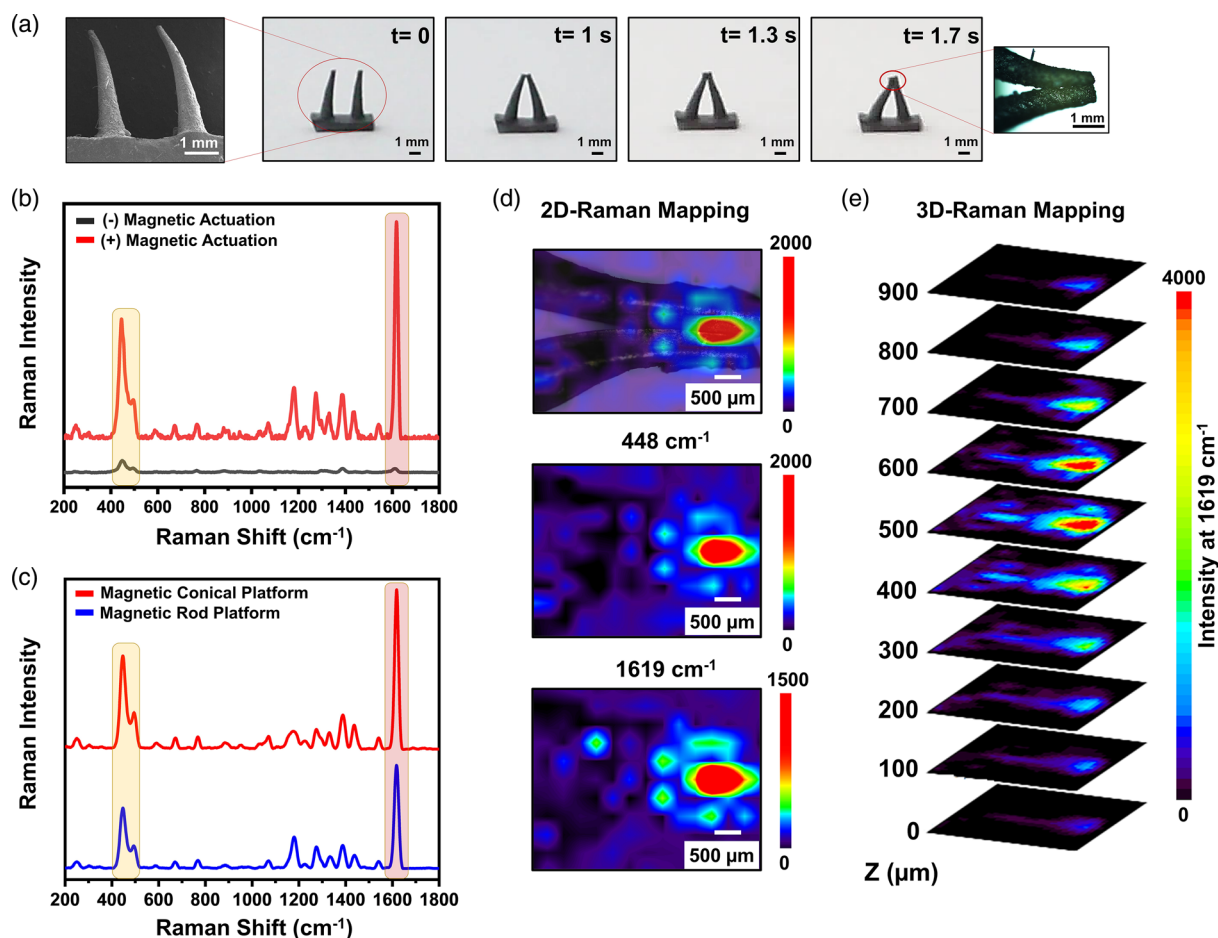
Figure 3. Conical magnetic actuator platforms and SERS performances. a) SEM image of a conical magnetic actuator platform and snapshots of the platform bending under 0.12 T magnetic field. b) SERS spectra of MB analyte (10^{-3} M) on the conical magnetic actuator platforms in the presence and absence of magnetic field (0.12 T). c) Comparative SERS spectra of MB analyte (10^{-3} M) on the conical (red spectrum) and cylindrical (blue spectrum) magnetic actuator platforms in the presence of magnetic field (0.12 T). d) 2D SERS Raman mapping of the bent conical magnetic actuator platforms for the 1619 and 448 cm^{-1} peaks of MB (The first figure is the overlaying figure that was produced using real platform pictures obtaining from Raman microscope and 2D SERS Raman mapping of the collected analyte molecules on the platforms for the 448 cm^{-1}). e) 3D Raman spatial mapping of the bent conical platform showing different focal planes along the z-axis.

conical platforms with a higher flexibility in the formation of hot-spots. The SERS performance of the conical platforms was investigated using MB in the presence and absence of a magnetic field. As shown in Figure 3b (black spectrum), prior to applying a magnetic field, the platform is SERS active but with a very low signal enhancement ability. In the presence of a magnetic field (red spectrum in Figure 3b), an impressive Raman signal enhancement was evident for the characteristic peaks of MB. For ν(C—C) ring stretches at 1621 cm^{-1}, the peak intensity was increased by 125-fold as compared to the original unbent conical platform. In accordance with our design goal, when compared with the cylindrical platform, the conical design provides $\approx$4.0-fold higher Raman signal enhancement (red versus blue spectra in Figure 3c). To better understand the difference between the conical and cylindrical platforms in the hot-spot formation performances, 2D and 3D Raman mapping processes were carried out by collecting more than 1000 Raman spectra from the joint point of the conical platform. As shown in Figure 3d, after magnetic actuation, the hot-spot formation occurs homogenously at the joint point spreading over an ellipse-shaped area with $\approx$1 mm diameter, which is $\approx$10$\times$ wider than the cylindrical platforms (round-shaped area with $\approx$250 µm diameter in Figure 2h). 3D Raman spatial mapping at 1619 cm^{-1} collected from different planes along the z-axis shows that the hot-spot generation occurs over a thickness of $\approx$500–600 µm along the z-axis (Figure 3e), which is again thicker than the cylindrical platforms ($\approx$100–200 µm depth in Figure 2i). It is evident that the current conical design gives not only much larger Raman enhancements as a result of enhanced electromagnetic fields but also a much larger volume of hot-spot formation for SERS analyses.
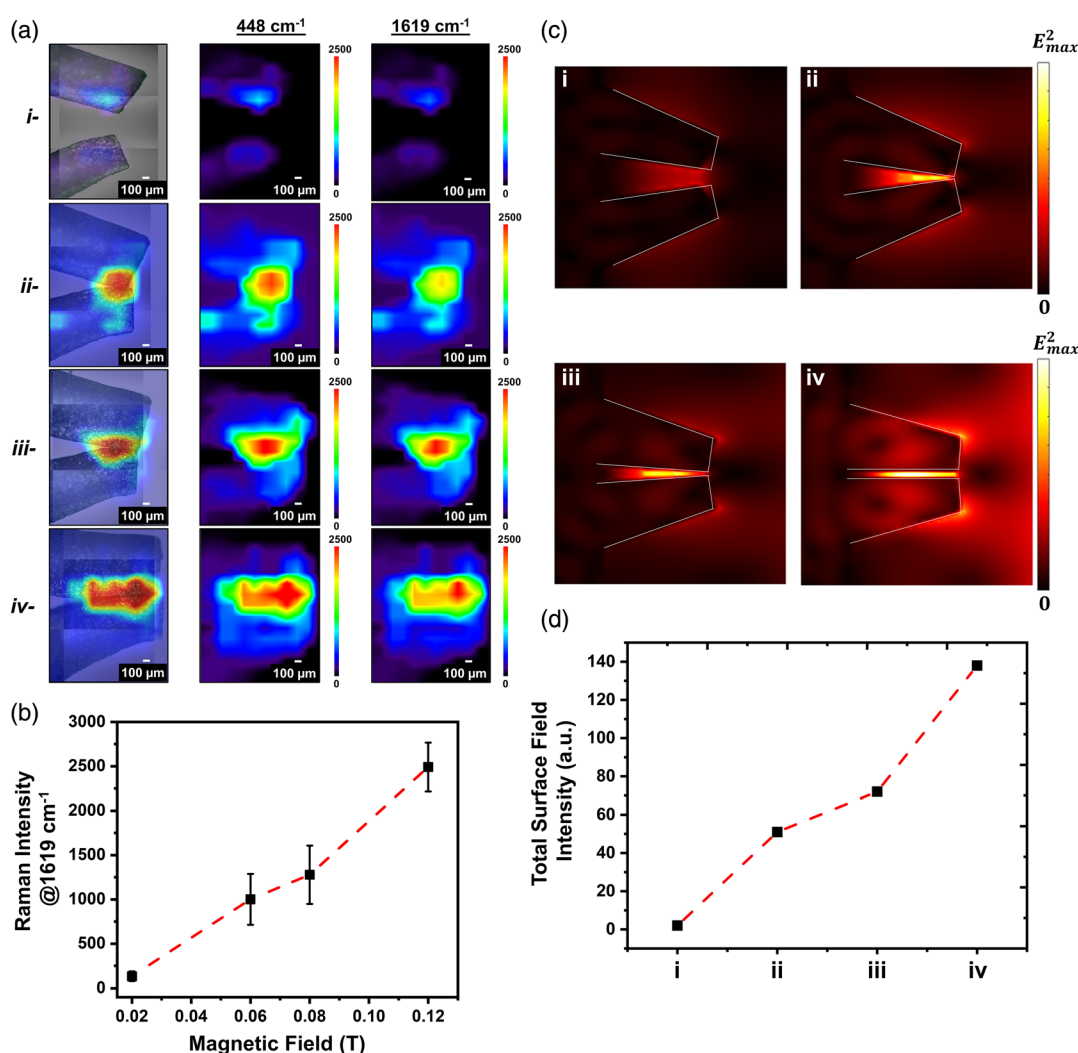

Figure 4. Experimental SERS performance of conical magnetic actuator platforms under different magnetic fields and theoretical finite difference time domain (FDTD) simulations. a) Experimental 2D SERS Raman mappings of the conical magnetic platforms under different magnetic fields using 10^{-3} M of MB analyte solution (i = 0.02 T, ii = 0.06 T, iii = 0.08 T, and iv = 0.12 T) (The first figures are the overlaying figure that was produced using real platform pictures obtaining from Raman microscope and 2D SERS Raman mapping of the collected analyte molecules on the platforms for the 448 cm^{-1}). b) Experimental Raman signal intensity of MB at 1619 cm^{-1} as a function of magnetic field. c) Cross-sectional profile for electric field intensity calculated for the conical platforms via FDTD simulations. d) Electric field intensity is calculated along the surface of the conical platforms under different configurations associated with different magnetic fields.

The role of the magnetic field on hot-spot formation was investigated by taking the 2D Raman mapping of MB at different frequencies on the conical platforms under varying magnetic field strengths (0.02–0.12 T). The conical arms do not form a physical contact when the magnetic field strength was 0.02 T (**Figure** 4a-i), and, therefore, Raman signals were collected only from the surface of the separated cones showing very low intensities. When the magnetic field strength is 0.06 T, a joint point with hot-spots was formed and substantial Raman signals were observed for MB (Figure 4a-ii). With the increased magnetic field strength to 0.08 T and 0.12 T, the hot-spot generation was dramatically enhanced spreading gradually over wider areas (Figure 4a-ii–iv). For the peak at 1619 cm^{-1}, the Raman signal enhancement under 0.12 T magnetic field was ≈2.5 times larger than that at 0.06 T (Figure 4b).

To reveal the phenomenon playing role in the gradual enhancement of Raman intensity with magnetic field, we performed FDTD simulations at the Raman laser excitation wavelength for different magnetic field intensities. In these simulations, we modeled the magnetic actuators as truncated cones and studied the four conditions (i–iv) shown in Figure 4a. In FDTD simulations (Lumerical Inc.), for the unit cell that consists

of two actuators, perfectly matched layer boundary condition was used along x-, y-, and z-axes, where the mesh size in all directions was chosen as 0.1 nm. As shown in Figure 4a, increasing the magnetic field intensity brings two tips closer; thus, we modeled either with two separated tips (i) or three tips (ii, iii, and iv), where we gradually decreased the angle in between. Figure 4c shows the cross-sectional profile of the electric field intensity, which demonstrates plasmonic hot-spots with large local electromagnetic fields. As shown in Figure 4, bringing two tips closer and decreasing angle in between clearly creates more hot-spots (Figure 4c-i,iv). Increasing Raman Intensity with magnetic field is directly related to strong light–matter interaction, which is due to accessible and large local electromagnetic fields.[48,56,57] To show the accessibility of these hot-spots in each magnetic actuator configuration, we calculated the total surface field intensity, which gives the sum of all the electric field intensity along the surface. Here, we defined a 3D field monitor and calculated the electric field intensity at the meshes right at the actuator surface of the 3D truncated cone-shaped actuators. As shown in Figure 4d, the total surface field intensity versus magnetic field profile for the present actuator configurations exhibits similar behavior to the Raman intensity versus magnetic field profile
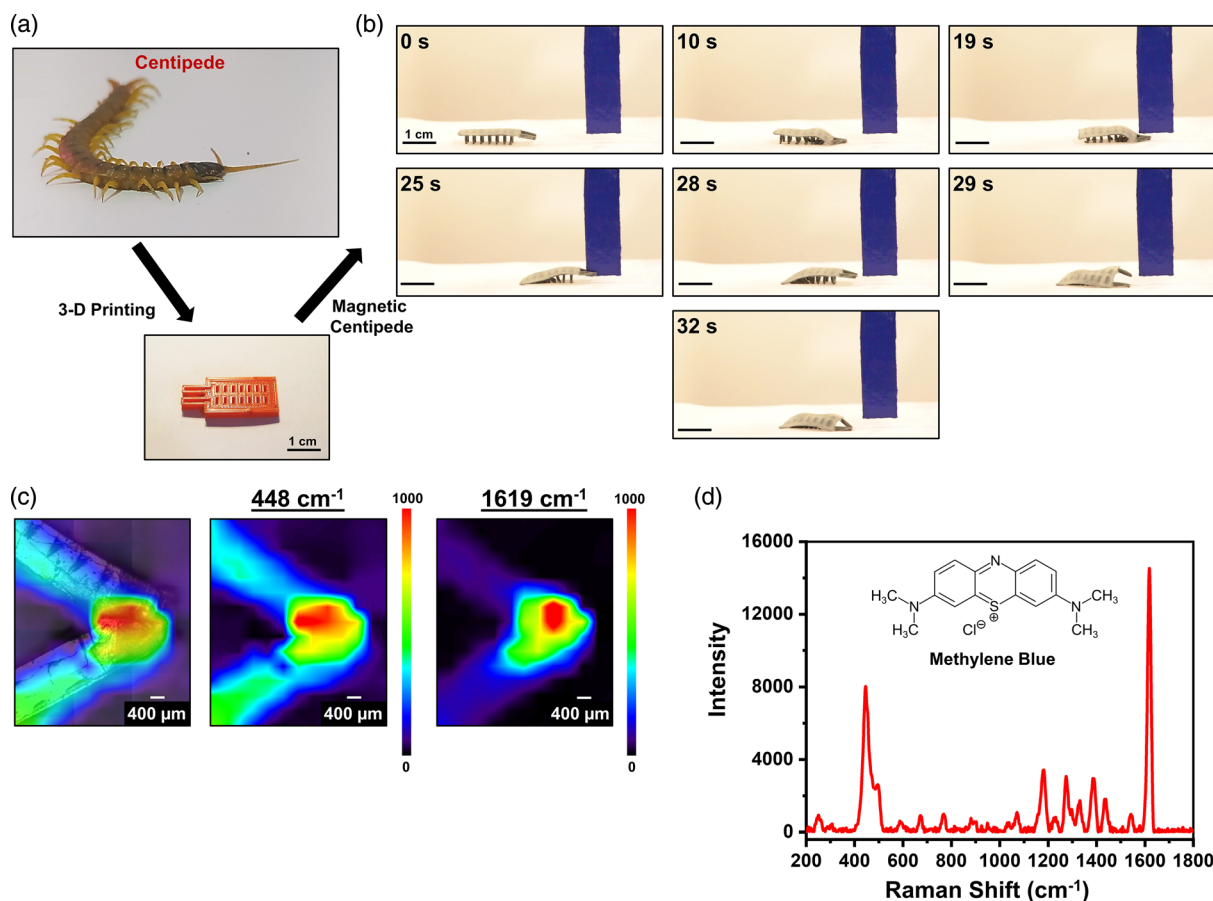
Figure 5. Centipede-inspired magnetic robot. a) Photo of a Turkish centipede. b) Snapshots of crawling and analyte collection (swapping) from MB (0.1 M) impregnated paper using centipede robot under 0.12 T magnetic field. c) 2D SERS Raman mapping of the collected analyte molecules on the centipede robot antennas for the 448 and 1619 cm^{-1} peaks (The first figure is the overlaying figure that was produced using real platform pictures obtaining from Raman microscope and 2D SERS Raman mapping of the collected analyte molecules on the platforms for the 448 cm^{-1}). d) SERS spectrum of the collected MB analyte molecules on the centipede robot antennas.

**ADVANCED
SCIENCE NEWS**

www.advancedsciencenews.com

**ADVANCED
INTELLIGENT
SYSTEMS**
Open Access

www.advintellsyst.com

(Figure 4b). This resemblance between the two profiles obviously shows that using a larger magnetic field that brings two actuators closer increases the number of hot-spots and makes them more accessible to strengthen light–matter interaction for stronger Raman intensities.

In the final part of our study, inspired by the Turkish centipede (**Figure 5**a), a proof-of-concept robotic demonstration is performed. We fabricated a platform with 2×8 magnetic cilia of 4 mm lengths and two antennas of 5 mm lengths using a 3D printed mold. In this platform, with the help of a magnetic field (0.12 T), while the cilia enable robotic motion, the antennas serve for analyte collection from a target point and subsequent hot-spot formation. In the fabrication of the centipede-inspired magnetic robot, a two-step molding process was carried out. First, iron microparticles and Ecoflex are mixed in 1:0.3 weight ratio, and the mixture was filled into the mold to form the legs and antennas. In the second step, Ecoflex without magnetic particles was poured into the mold to form the robot's body. Finally, the magnetic antennas were decorated with AuNPs as described earlier (vide supra). A filter paper impregnated with aqueous solution of MB analyte (0.1 M) was employed as the model target. In the experiment, the centipede-inspired robot first moves to the target area through controlling magnetic field, and, subsequently, analyte molecules from the target are transferred to the AuNP decorated antennas with a simple swab motion (Figure 5b at 25 s and Movie S3, Supporting Information). After collecting the analyte molecules, the antennas were bent to generate the desired hot-spots (Figure 5b at 32 s). Figure 5c shows the 2D Raman mapping, which indicates that the analyte molecules were successfully collected and the hot-spots were generated at the joint points after the bending process. The corresponding Raman spectrum for the collected analyte molecules is shown in Figure 5d.

3. Conclusion

Realizing the optimal structural configuration for hot-spot generation is the key parameter for achieving large electromagnetic field enhancements in plasmonic applications. Conventional methods to yield such enhancements are based on the controlling optical responses of structures in a static manner, for example, by varying their geometrical shapes or the properties of the constituting materials. However, fabricating the ideal structure that supports an optical response matching with that of the incident light allowing the strongest light–matter interaction is challenging due to fabrication tolerances. Therefore, there is a strong need for active devices that enable dynamic tuning of hot-spot locations through external mechanisms. In that sense, we have developed cilia-inspired soft plasmonic platforms that are capable of forming highly accessible millimeter-sized hot-spots via bending motion under a magnetic field. The manipulation of the hot-spot formation was achieved by using different cilia designs and magnetic field strengths, which enabled remarkable Raman signal enhancement performances of up to $\approx$120-fold compared to the unactuated form. To show the potential of our strategy in a real-life application, a centipede-inspired robotic platform was demonstrated to collect/detect molecular targets by controlling the platform motion and hot-spot formation via

magnetic field. Creating such large local electromagnetic fields extensively extending within the medium in the vicinity, our platform could be also used for label-free sensing of small molecules, for example, protein molecules or drug molecules, or large microorganisms, for example, viruses or bacteria, while collecting these targeted analytes. Possessing the ability to create and control the hot-spot locations dynamically, we could apply our technique for remote biosensing using plasmonic structures. This modality could open doors for new strategies, for example, targeted delivery of analytes that could be critical for sensing-by-binding platforms. Since analyte molecules were drop-casted onto one of the cilia arms and hot-spots were formed later via bending motion, certain molecules, especially structurally rigid and sizeable ones that cannot orient itself into preformed hot-spots, could be analyzed with ease. Another important advantage of our platform is that each arm could be separately decorated with different types of plasmonic materials (e.g., different metals or different shapes), which allow for the fundamental hot-spot studies that are controllably formed between different plasmonic particles. Contrary to conventional hot-spot engineering strategies, we believe that the demonstrated approach brings new exciting opportunities not only for sensing but also for other diverse applications including plasmonic catalysis, energy generation, and even homeland security.

4. Experimental Section

Fabrication of Platforms: Cilia-inspired magnetic actuators were fabricated using 3D-printed molds. Two different molds designs were used in this work [i.e., conical molds (cone length = 4.0 and 5.0 mm, and distance between cones = 1.6, 2.0 and 2.4 mm) and cylindrical molds (cylinder length = 4.0 mm and distance = 1.6 mm, antenna length = 5 mm)]. Conical molds were first built using the 3D Builder software (Microsoft, USA) with various shapes and sizes, and then converted into G-codes using Cura software (Ultimaker, Netherlands). They were finally printed using poly(lactic acid) (PLA) (eSUN, China) filaments with a fused deposition modeling (FDM) printer (Ultimaker2+). Printing parameters were: 0.4 mm nozzle diameter, 40 mm s^{-1} printing speed, and 20% infill density. For cylindrical platforms, a master model was first designed using the same software but sliced with PreForm software (Formlabs, USA) and was printed with a stereolithography (SLA)) printer (Formlabs Form-2) with 100 μ resolution using FormLabs' white resin v4. Centipede-inspired robots were also fabricated similar to cylindrical molds.

After printing, all supporting materials were removed from the molds, and then coated with a thin layer of lubricant (Mann Ease Release 200, Smooth-on Inc.). A mixture of Ecoflex (00-30, Smooth-on Inc.) and magnetic Fe particles ($\approx$5.0 μm in diameter, Nanokar, Turkey) were mixed in a 1:0.3 weight ratio and filled into molds. We chose magnetic microparticles in our work due to their low cost and easy handling. After the mixture was cured in an oven, the platforms were peeled off the molds without damaging. For the fabrication of conical platforms, Eco-flex was first poured over master molds. After curing and peeling off, conical magnetic actuators were formed into the Eco-flex molds similar to cylindrical platforms. All magnetic actuation experiments were carried out using permanent magnets ($B = 0.02$–0.12 T). Actuating performance of all samples was recorded by a Canon EOS 650D camera. The bending angles were also calculated via IMAGEJ software.

To decorate platforms with plasmonic AuNPs, they were first immersed into a dopamine solution [dopamine hydrochloride (Sigma H8502), 2.0 mg mL^{-1} in 10^{-3} M Tris buffer, pH 8.5] at room temperature. After 3 h, the platforms were washed with DI-water and dried with N$_2$ gas. Finally, PDOP-coated platforms were immersed into an aqueous AuNP solution (1.83×10^{-9} M) for 24 h. The synthesis of AuNPs was given elsewhere.[50]

SERS Experiments: Raman characteristics of magnetic platforms were investigated using a high-resolution confocal Raman spectrometer (Jasco NRS-4500, Japan) with an excitation wavelength of 785 nm and an operational range of 200–2000 cm^{-1}. Unless otherwise specified, all Raman spectra were collected under the same experimental conditions (i.e., ×20 microscope objective with a 3 µm laser spot size, 75 mW laser power, and 30 s acquisition time). In measurements, four different molecules (i.e., MB, R6G, CV, and MG) were used as reporter molecules. In a typical experiment, 5.0 µL aqueous solution of analyte with a concentration of 10^{-3} M was dripped onto actuator surface followed by storing in a hood at room temperature until dry. Raman spectra were subsequently collected from at least 10 different spots across the entire dried area for each sample.

Supporting Information

Supporting Information is available from the Wiley Online Library or from the author.

Conflict of Interest

The authors declare no conflict of interest.

Author Contributions

G.D. and H.U. conceived and designed the experiments. G.L., E.E., and P.Y.H. fabricated molds and platforms. A.E.C. designed and performed the theoretical calculations. E.Y., G.L., and K.O.H. performed the SERS experiments. G.D., H.U., and A.E.C. cowrote the paper. All authors discuss the results and commented on the manuscript.

Data Availability Statement

The data that support the findings of this study are available from the corresponding author upon reasonable request.

[1] W. Feng, A. M. Newbigging, C. Le, B. Pang, H. Peng, Y. Cao, J. Wu, G. Abbas, J. Song, D.-B. Wang, *Anal. Chem.* **2020**, *92*, 10196.

[2] O. Vandenberg, D. Martiny, O. Rochas, A. van Belkum, Z. Kozlakidis, *Nat. Rev. Microbiol.* **2021**, *19*, 171.

[3] C. S. Goldberg, D. S. Pilliod, R. S. Arkle, L. P. Waits, *PloS One* **2011**, *6*, e22746.

[4] S. Humbert, S. Tarnawski, N. Fromin, M.-P. Mallet, M. Aragno, J. Zopfi, *ISME J.* **2010**, *4*, 450.

[5] N. Kayaci, R. Ozdemir, M. Kalay, N. B. Kiremitler, H. Usta, M. S. Onses, *Adv. Funct. Mater.* **2022**, *32*, 2108675.

[6] Z. Li, G. Wang, Y. Ye, B. Li, H. Li, B. Chen, *Angew. Chem. Int. Ed.* **2019**, *131*, 18193.

[7] N. B. Colthup, L. H. Daly, S. E. Wiberley, *Introduction to Infrared and Raman Spectroscopy*, Academic Press, London **1990**.

[8] P. L. Stiles, J. A. Dieringer, N. C. Shah, R. P. Van Duyne, *Annu. Rev. Anal. Chem.* **2008**, *1*, 601.

[9] G. Demirel, H. Usta, M. Yilmaz, M. Celik, H. A. Alidagi, F. Buyukserin, *J. Mater. Chem. C* **2018**, *6*, 5314.

[10] X. Wang, S.-C. Huang, S. Hu, S. Yan, B. Ren, *Nat. Rev. Phys.* **2020**, *2*, 253.

[11] A. I. Pérez-Jiménez, D. Lyu, Z. Lu, G. Liu, B. Ren, *Chem. Sci.* **2020**, *11*, 4563.

[12] R. Aroca, *Surface-Enhanced Vibrational Spectroscopy*, John Wiley & Sons, New York, NY **2006**.

[13] B. Sharma, R. R. Frontiera, A.-I. Henry, E. Ringe, R. P. Van Duyne, *Mater. Today* **2012**, *15*, 16.

[14] G. C. Schatz, M. A. Young, R. P. V. Duyne In *Surface-Enhanced Raman Scattering* (Eds: K. Kneipp, M. Moskovits, H. Kneipp), Springer, Berlin **2006**, pp. 19–45.

[15] S.-Y. Ding, E.-M. You, Z.-Q. Tian, M. Moskovits, *Chem. Soc. Rev.* **2017**, *46*, 4042.

[16] S. L. Kleinman, R. R. Frontiera, A.-I. Henry, J. A. Dieringer, R. P. Van Duyne, *Phys. Chem. Chem. Phys.* **2013**, *15*, 21.

[17] K. Sivashanmugan, J.-D. Liao, J.-W. You, C.-L. Wu, *Sens. Actuators B Chem.* **2013**, *181*, 361.

[18] S. Simoncelli, E.-M. Roller, P. Urban, R. Schreiber, A. J. Turberfield, T. Liedl, T. Lohmuller, *ACS Nano* **2016**, *10*, 9809.

[19] H. Li, P. Merkl, J. Sommertune, T. Thersleff, G. A. Sotiriou, *Adv. Sci.* **2022**, *9*, 2201133.

[20] H. K. Lee, Y. H. Lee, C. S. L. Koh, G. C. Phan-Quang, X. Han, C. L. Lay, H. Y. F. Sim, Y.-C. Kao, Q. An, X. Y. Ling, *Chem. Soc. Rev.* **2019**, *48*, 731.

[21] H.-Y. Chen, M.-H. Lin, C.-Y. Wang, Y.-M. Chang, S. Gwo, *J. Am. Chem. Soc.* **2015**, *137*, 13698.

[22] B. Sharma, M. F. Cardinal, S. L. Kleinman, N. G. Greeneltch, R. R. Frontiera, M. G. Blaber, G. C. Schatz, R. P. Van Duyne, *MRS Bull.* **2013**, *38*, 615.

[23] M. Li, Y. Tang, R. H. Soon, B. Dong, W. Hu, M. Sitti, *Sci. Adv.* **2022**, *8*, abm5616.

[24] M. Li, A. Pal, A. Aghakhani, A. Pena-Francesch, M. Sitti, *Nat. Rev. Mater.* **2022**, *7*, 235.

[25] B. Chen, Z. Shao, Z. Xie, J. Liu, F. Pan, L. He, L. Zhang, Y. Zhang, X. Ling, F. Peng, *Adv. Intell. Syst.* **2021**, *3*, 2000251.

[26] Y. Roh, M. Kim, S. M. Won, D. Lim, I. Hong, S. Lee, T. Kim, C. Kim, D. Lee, S. Im, *Sci. Robot.* **2021**, *6*, abi6774.

[27] J. Mersch, M. Bruns, A. Nocke, C. Cherif, G. Gerlach, *Adv. Intell. Syst.* **2021**, *3*, 2000221.

[28] Y. Zhao, C.-Y. Lo, L. Ruan, C.-H. Pi, C. Kim, Y. Alsaid, I. Frenkel, R. Rico, T.-C. Tsao, X. He, *Sci. Robot.* **2021**, *6*, abd5483.

[29] G. Demirel, Z. Rzaev, S. Patir, E. Pişkin, *J. Nanosci. Nanotechnol.* **2009**, *9*, 1865.

[30] R. S. Diteesawat, T. Helps, M. Taghavi, J. Rossiter, *Sci. Robot.* **2021**, *6*, abc3721.

[31] K. Wang, L. W. Yap, S. Gong, R. Wang, S. J. Wang, W. Cheng, *Adv. Funct. Mater.* **2021**, *31*, 2008347.

[32] W. Tang, Y. Lin, C. Zhang, Y. Liang, J. Wang, W. Wang, C. Ji, M. Zhou, H. Yang, J. Zou, *Sci. Adv.* **2021**, *7*, abf8080.

[33] Y. Ling, W. Pang, J. Liu, M. Page, Y. Xu, G. Zhao, D. Stalla, J. Xie, Y. Zhang, Z. Yan, *Nat. Commun.* **2022**, *13*, 524.

**ADVANCED
SCIENCE NEWS**

www.advancedsciencenews.com

**ADVANCED
INTELLIGENT
SYSTEMS**

www.advintellsyst.com

[34] N. Ebrahimi, C. Bi, D. J. Cappelleri, G. Ciuti, A. T. Conn, D. Faivre, N. Habibi, A. Hošovský, V. Iacovacci, I. S. Khalil, *Adv. Funct. Mater.* **2021**, *31*, 2005137.

[35] N. El-Atab, R. B. Mishra, F. Al-Modaf, L. Joharji, A. A. Alsharif, H. Alamoudi, M. Diaz, N. Qaiser, M. M. Hussain, *Adv. Intell. Syst.* **2020**, *2*, 2000128.

[36] H. Gu, Q. Boehler, H. Cui, E. Secchi, G. Savorana, C. De Marco, S. Gervasoni, Q. Peyron, T.-Y. Huang, S. Pane, *Nat. Commun.* **2020**, *11*, 2637.

[37] H. Gu, Q. Boehler, D. Ahmed, B. J. Nelson, *Sci. Robot.* **2019**, *4*, aax8977.

[38] T. Jiralerspong, G. Bae, J.-H. Lee, S.-K. Kim, *ACS Nano* **2020**, *14*, 17589.

[39] Y. Kim, H. Yuk, R. Zhao, S. A. Chester, X. Zhao, *Nature* **2018**, *558*, 274.

[40] T. Xu, J. Zhang, M. Salehizadeh, O. Onaizah, E. Diller, *Sci. Robot.* **2019**, *4*, aav4494.

[41] Y. Kim, X. Zhao, *Chem. Rev.* **2022**, *122*, 5317.

[42] B. Han, Z. C. Ma, Y. L. Zhang, L. Zhu, H. Fan, B. Bai, Q. D. Chen, G. Z. Yang, H. B. Sun, *Adv. Funct. Mater.* **2022**, *32*, 2110997.

[43] P. Karipoth, A. Christou, A. Pullanchiyodan, R. Dahiya, *Adv. Intell. Syst.* **2022**, *4*, 2100092.

[44] T. E. Greenwood, H. Cagle, B. Pulver, O. S. Pak, Y. L. Kong, *Adv. Intell. Syst.* **2022**, *4*, 2200166.

[45] Q. Jin, M. Li, B. Polat, S. K. Paidi, A. Dai, A. Zhang, J. V. Pagaduan, I. Barman, D. H. Gracias, *Angew. Chem. Int. Ed.* **2017**, *129*, 3880.

[46] W. Xu, S. K. Paidi, Z. Qin, Q. Huang, C.-H. Yu, J. V. Pagaduan, M. J. Buehler, I. Barman, D. H. Gracias, *Nano Lett.* **2018**, *19*, 1409.

[47] S. Lanzalaco, P. Gil, J. Mingot, A. Àgueda, C. Alemán, E. Armelin, *ACS Biomater. Sci. Eng.* **2022**, *8*, 3329.

[48] G. Liman, E. Yildiz, H. Ilhan, A. E. Cetin, G. Demirel, *Adv. Opt. Mater.* **2021**, *9*, 2100009.

[49] Q. Peyron, Q. Boehler, K. Rabenorosoa, B. J. Nelson, P. Renaud, N. Andreff, *IEEE Robot. Autom. Lett.* **2018**, *3*, 3646.

[50] J. Kimling, M. Maier, B. Okenve, V. Kotaidis, H. Ballot, A. Plech, *J. Phys. Chem. B* **2006**, *110*, 15700.

[51] M. S. Akin, M. Yilmaz, E. Babur, B. Ozdemir, H. Erdogan, U. Tamer, G. Demirel, *J. Mater. Chem. B* **2014**, *2*, 4894.

[52] M. Yilmaz, G. Bakirci, H. Erdogan, U. Tamer, G. Demirel, *RSC Adv.* **2016**, *6*, 12638.

[53] G. Demirel, R. L. Gieseking, R. Ozdemir, S. Kahmann, M. A. Loi, G. C. Schatz, A. Facchetti, H. Usta, *Nat. Commun.* **2019**, *10*, 5502.

[54] I. Deneme, G. Liman, A. Can, G. Demirel, H. Usta, *Nat. Commun.* **2021**, *12*, 6119.

[55] M. Yilmaz, E. Babur, M. Ozdemir, R. L. Gieseking, Y. Dede, U. Tamer, G. C. Schatz, A. Facchetti, H. Usta, G. Demirel, *Nat. Mater.* **2017**, *16*, 918.

[56] A. E. Cetin, D. Etezadi, H. Altug, *Adv. Opt. Mater.* **2014**, *2*, 866.

[57] A. E. Cetin, C. Yilmaz, B. C. Galarreta, G. Yilmaz, H. Altug, A. Busnaina, *Plasmonics* **2020**, *15*, 1165.